Dynamic EAF Energy and Material Balance Model for On-Line Process Optimization

Digital technologies are transforming industry at all levels. Steel has the opportunity to lead all heavy industries as an early adopter of specific digital technologies to improve our sustainability and competitiveness. This column is part of AIST's strategy to become the epicenter for steel's digital transformation, by providing a variety of platforms to showcase and disseminate Industry 4.0 knowledge specific for steel manufacturing, from big-picture concepts to specific processes.

Authors

Sunday Abraham
Director R&D, SSAB Americas, Muscatine, Iowa, USA
sunday.abraham@ssab.com

Yufeng Wang
Senior Research Engineer, SSAB Americas, Muscatine, Iowa, USA
yufeng.wang@ssab.com

Randy Petty
Superintendent, Primary Operations, SSAB Americas, Muscatine, Iowa, USA
randy.petty@ssab.com

Tim Sprague
Manager, Melting, SSAB Americas, Muscatine, Iowa, USA
tim.sprague@ssab.com

Tony Franks
EAF Project Engineer, SSAB Americas, Muscatine, Iowa, USA
tony.franks@ssab.com

Eric Brown
Master Black Belt, Six Sigma, SSAB Americas, Muscatine, Iowa, USA
eric.brown@ssab.com

The discovery of electric arc by Sir Humphry Davy, a British chemist, in 1800 led to the invention of the electric arc furnace.[1] In 1853, primitive forms of the electric arc furnace were developed in France and England. In 1878, Sir William Siemens patented an electric arc furnace that operated using dynamo as a source of current. Initially, electric arc furnaces were used for the production of alkali metals, phosphorus, graphite, calcium carbides and metallic calcium. In 1886, Paul Héroult of France was granted a patent for the electric arc furnace used for the production of aluminum. In 1896, Major Stassano of Italy began making electric arc furnaces for smelting iron ores. At this time, the prices of electricity were prohibitive, and the production of iron using Stassano's electric arc furnace did not amount to any degree of commercial success, as it could not compete with the blast furnace and open-hearth processes. A breakthrough in the commercialization of the electric arc furnace for steelmaking occurred in 1906. During this time, the Canadian government collaborated with Paul Héroult of France to conduct a series of experiments at Sault Ste. Marie to smelt Canadian iron ore in Héroult's electric arc furnace. The success of this collaboration set the stage for the rapid growth of using electric arc furnaces for the production of pig iron. However, the tonnage from the electric arc furnaces was very low (typically, 1–15 tons), and therefore, their use was reserved for producing special steels because it was not economical for bulk steel production. The output from the electric arc furnace steelmaking process was limited because significant aspects of the operation were conducted manually. In the 1950s, however, technological advancements in furnace designs and improved electrode controls increased the efficiency of the electric arc furnace steelmaking process. This resulted in the continued expansion of the use of the electric arc furnace for steelmaking.[2,3]

The electric arc steelmaking process is particularly attractive due to its low capital cost compared to the traditional (blast furnace) route of steelmaking. Other advantages of electric arc furnace route of steelmaking are: (a) simplicity of the plant operation; (b) flexibility to produce a variety of grades; (c) better environmental impact; and (d) possibility of using local energy sources. These benefits are the reasons for the emergence of the electric arc furnace as the dominant steelmaking route today. Table 1 provides a summary of the technological advancements that contributed to the success of electric arc furnace steelmaking process.[4] Although significant improvement in operational efficiency of electric arc furnace has been achieved over the last few decades thanks to the automation of control systems,[5–12] the control of the metallurgical aspects of the process is still based on the judgment of individual operators. One area that can be beneficial to the operation of the EAF is application of mathematical modeling. Many studies have been conducted in the academic community regarding modeling of the EAF steelmaking process over the last few decades. These modeling initiatives include the applications of computational fluid dynamics (CFD), thermodynamic analysis and, more recently, machine learning (artificial intelligence).[13–38] These models are often not tailored for

Table 1

Technological Development for the Electric Arc Furnace (EAF) Steelmaking Process

Technology	Benefits
Ultrahigh-power system in 1950s	(a) Arc stability and (b) reduction of melting time
Automated electrode positioning in 1950s	Reduction in cost of electricity
Oxygen lancing and carbon injection in mid-1970s	(a) Slag foaming; (b) decreased arc radiation; (c) decreased power loss; (d) decreased refractory wear; and (e) increased yield
Eccentric bottom tapping (EBT) in 1985	(a) Shorter tap-to-tap time; (b) reduced slag carryover; (c) compact stream; (d) lower EAF tilting angle during tapping; and (e) improved power efficiency with shorter length of water-cooled power cable
Fuchs shaft furnace for scrap pre-heating in 1980s	(a) Reduction of NOx; (b) reduction of heat loss; and (c) improved energy efficiency
Consteel system for scrap pre-heating in 1992	(a) Reduction of NOx; (b) reduction of heat loss; and (c) improved energy efficiency
Coherent supersonic oxygen jet and burner system in late 1990s	(a) Oxygen utilization efficiency; (b) intense decarburization; (c) improved slag foaming; and (d) reduced power consumption

use for on-line process optimization because some of them deal only with specific segments of the process while others do not provide the necessary user-friendly outputs for use by operators.

Only about 55–65% of the energy supplied is utilized for melting the scrap in the EAF steelmaking process. The remainder of the energy is lost to slag, EAF refractory, cooling system and offgases. Further incremental improvement in the energy efficiency during steelmaking can be realized by ensuring consistency of operation through the application of predictive thermodynamic models.

The purpose of the study discussed in this paper was to develop a model suitable for on-line process optimization to ensure consistency and more efficient operation of the EAF. The paper discusses the development and implementation of a comprehensive energy and material balance model for predicting key melting parameters, including temperature, carbon, oxygen, slag composition and the concentrations of other elements. The application of the model to the EAF steelmaking process has resulted in improved energy efficiency and productivity by reducing delays in the operation of twin EAF furnace operation at SSAB Iowa.

Modeling Concept

The model comprises several submodels, as depicted in Fig. 1. The concepts employed in the development of each submodel are described next.

Bath Temperature Prediction Module — The energies provided for the EAF process are used in heating the scrap and slag formers (lime and dolo-lime) to their melting points, melting of the scrap and slag formers, and heating the liquid iron and slag to the required

Figure 1

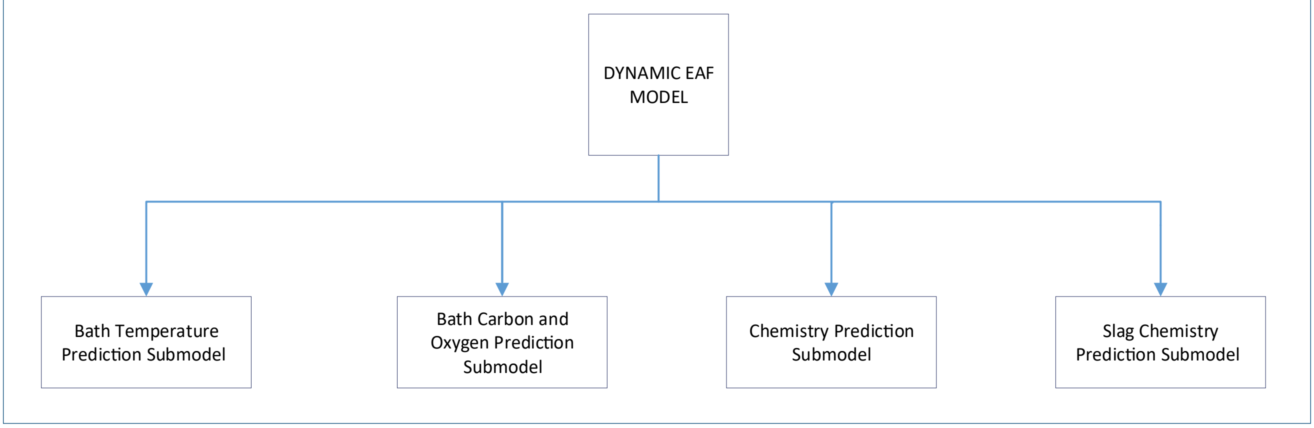

Different submodels of the energy and material balance model.

tap temperature. The melting process can be written in general form as in Eq. 1.

$$E_{req} = C_m M_{m_i}(T_m - T_0) + M_{m_i} L_{mh} + C_l M_{m_i}(T - 1806) + C_s M_{s_i}(T_s - T_0) + M_{s_i} L_{sh} + C_{ls} M_{s_i}(T - 1573)$$

(Eq. 1)

where

E_{req} = energy required,
C_m = specific heat capacity of iron at a constant pressure,
M_{m_i} = melting rate of scrap,
T_m = melting point of iron,
C_l = specific heat capacity of liquid iron at a constant pressure,
L_{mh} = latent heat of melting of iron,
C_s = specific heat capacity of slag at a constant pressure,
C_{ls} = specific heat capacity of molten slag at a constant pressure,
M_{s_i} = melting rate of slag,
T_s = melting point of slag,
T_0 = initial bath temperature prior to commencement of melting, which is ≥293 K, if there is no hot heel and
L_{sh} = latent heat of melting of slag.

The impact of furnace hot heel on the energy and material balance was accounted for by considering the heel to be at the temperature of the previously tapped heat. The specific heat capacity of a given material is a function of temperature.[39] The values of specific heat capacities of solid iron, liquid iron, solid slag and liquid slag used in the development of the model were taken from different sources.[13,14,39]

The energies available for melting at any given time can be written as shown in Eq. 2:

$$E_{inp} = E_{P_i} + E_{C_i}$$

(Eq. 2)

where

E_{inp} = energy input,
E_{P_i} = energy from electricity and
E_{C_i} = energy from chemical reactions.

The chemical reactions comprise combustion of natural gas and carbon, and exothermic reactions involving oxygen and the dissolved elements. The combustion of natural gas proceeds per the reaction in Eq. 3:

$$CH_4 + 2O_2 \rightarrow CO_2 + 2H_2O$$

(Eq. 3)

The combustion of carbon can proceed per the reactions in Eqs. 4 and 5:

$$[C] + \frac{1}{2}O_2 \rightarrow CO$$

(Eq. 4)

$$CO + \frac{1}{2}O_2 \rightarrow CO_2$$

(Eq. 5)

The reaction shown by Eq. 5 can only proceed if there is sufficient oxygen available for the reaction, but the instability of CO_2 at high temperatures limits the extent of such reaction.

The other exothermic reactions considered in this model are:

$$Fe + \frac{1}{2}O_2 \rightarrow FeO$$

(Eq. 6)

$$[Mn] + \frac{1}{2}O_2 \rightarrow MnO$$

(Eq. 7)

$$[Si] + O_2 \rightarrow SiO_2$$

(Eq. 8)

$$2[Al] + \frac{3}{2}O_2 \rightarrow Al_2O_3$$

(Eq. 9)

When in the burner mode, the ratio of the flowrate of oxygen to that of the natural gas is typically at stoichiometric value (2:1), and therefore, all of the supplied oxygen goes into a reaction with the natural gas. When in the lancing mode, the distribution of oxygen for the exothermic reactions were based on Eqs. 10–15. The amount of oxygen used for the oxidation of carbon is first determined per Eq. 10. When the carbon content of the bath is high, most of the supplied oxygen is considered to be utilized for the oxidation of carbon. The utilization of oxygen for combustion of carbon can be expressed as in Eq. 10:

$$n_{C-CO_i}^{O_2} < n_i^{O_2}$$

(Eq. 10)

where

$n_{C-CO_i}^{O_2}$ = number of moles of oxygen involved in combustion of carbon to carbon monoxide at any given time and
$n_i^{O_2}$ = number of moles of supplied oxygen.

Therefore, Eq. 11 needs to be solved to determine how much oxygen is available for other exothermic reactions.

$$\Delta n_i^{O_2} = n_i^{O_2} - n_{C-CO_i}^{O_2} > 0$$

(Eq. 11)

where $\Delta n_i^{O_2}$ is the number of moles of excess oxygen at any given time. Eqs. 12–15 need to be solved to determine the distribution of excess oxygen for other exothermic reactions.

$$\Delta n_i^{O_2} = \alpha_{SiO_2}\Delta n_i^{O_2} + \alpha_{Al_2O_3}\Delta n_i^{O_2} + \alpha_{FeO}\Delta n_i^{O_2} + \alpha_{MnO}\Delta n_i^{O_2}$$

(Eq. 12)

where α is the coefficient of utilization of excess oxygen for exothermic reaction.

$$\alpha_{SiO_2} + \alpha_{Al_2O_3} + \alpha_{FeO} + \alpha_{MnO} = 1$$

(Eq. 13)

$$\alpha_{SiO_2} > \alpha_{Al_2O_3}$$

(Eq. 14)

$$\alpha_{FeO} = \alpha_{MnO} < \alpha_{Al_2O_3}$$

(Eq. 15)

Therefore, if the excess oxygen is known, the distribution of oxygen for the exothermic reactions can be determined, and hence, the concentrations of Mn, Si and Al in the bath can be estimated at any given time during the melting and refining processes. The starting concentrations of these elements are determined from the chemistries of the scrap. The concentration of carbon is determined based on the supplied amount of charged and injection carbon, and concentrations of carbon in the scrap.

Thus, the total chemical energy available for scrap melting at any given time is a sum of all the energies from all of the above sources, as shown in Eq. 16.

$$E_{C_i} = E_{CO_2 + H_2O_i} + E_{CO_i} + E_{CO_{2i}} + E_{FeO_i} + E_{MnO_i} + E_{SiO_{2i}} + E_{Al_2O_{3i}}$$

(Eq. 16)

The energy from the combustion of natural gas is determined per Eq. 17:

$$E_{CH_4} = n_{CH_4}\Delta H_{CO_2 + H_2O}$$

(Eq. 17)

where

n_{CH_4} = moles of natural gas supplied and
$\Delta H_{CO_2 + H_2O}$ = the enthalpy of combustion of natural gas.

The energy for other exothermic reactions are determined by Eq. 18:

$$E_{R_xO_y} = \frac{x}{y}\alpha_{R_xO_y}\Delta n_i^{O_2}\Delta H_{R_xO_y}$$

(Eq. 18)

where

R = C, Fe, Si, Al and Mn and
$\Delta H_{R_xO_y}$ = enthalpy of reaction of a given element with oxygen.

The total energy available for scrap melting at any given time can be written, as in Eq. 19:

$$E_{P_i} + E_{C_i} = E_{P_i} + E_{CO_2 + H_2O_i} + E_{CO_i} + E_{CO_{2i}} + E_{FeO_i} + E_{MnO_i} + E_{SiO2_i} + E_{Al2O3_i}$$

(Eq. 19)

The complete energy and material balance for scrap melting and refining processes in the EAF can thus be written, as in Eq. 20:

$$\left(C_m\left(T_m - T_0\right) + L_{mh} + C_l\left(T - 1806\right)\right)\sum_{i=1}^{n} M_{m_i} + \left(C_s\left(T_s - T_0\right) + L_{sh} + C_{ls}\left(T - 1573\right)\right)\sum_{i=1}^{m} M_{S_i} = \eta\left(\begin{array}{l}\sum_{i=1}^{z} E_{P_i} + \sum_{i=1}^{j} E_{CO_2+H_2O_i} + \sum_{i=1}^{k} E_{CO} + \sum_{i=1}^{h} E_{CO_{2i}} + \\ \sum_{i=1}^{l} E_{FeO_i} + \sum_{i=1}^{u} M_{MnO_i} + \sum_{i=1}^{p} E_{SiO_{2i}} + \sum_{i=1}^{q} Al_2O_{3i}\end{array}\right)$$

(Eq. 20)

where

η = the coefficient of energy utilization for scrap melting for a given heat. Its value is always <1 and
i = time.

The coefficient of energy utilization for a given heat is a function of the coefficients of utilization of energy for individual scrap. The coefficient of energy utilization for a given scrap is dependent on its chemistry and surface area. Scrap with higher surface area will melt faster. Therefore, for a given heat, the coefficient of energy utilization for a given heat can be expressed, as in Eq. 21:

$$\eta = \sum_{i=1}^{n} \eta_i f_{c_i}$$

(Eq. 21)

where

n = number of scrap types,
η_i = coefficient of utilization of energy for a given scrap when $f_{c_i} = 1$ and
f_{c_i} = fraction of a given scrap in the metallic charge for a given heat.

Melting is complete and refining begins when Eq. 22 holds.

$$\sum_{i=1}^{n} M_{m_i} = \chi \sum_{i=1}^{j} f_{c_i}^{Fe} M_{c_i}$$

(Eq. 22)

where

M_{c_i} = weight of a given scrap type,
$f_{c_i}^{Fe}$= fraction of Fe in the scrap and
χ = recovery rate of iron from the scrap.

Bath Carbon and Oxygen Contents — Typically, in the EAF steelmaking process where scrap is recycled, carbon can be supplied in two forms: charge carbon and injection carbon. The charge carbon is added along with the scrap in the bucket, and during refining, the injection carbon is supplied through carbon injectors from the burner systems mounted on the wall. The charge carbon is typically supplied in the form of metallurgical coke and anthracite coal, which contains about 88–90% carbon. The charge carbon is primarily intended to provide chemical energy per the reaction in Eq. 4 and remove nitrogen from the bath via the evolving bubbles of CO. Also, the evolving CO from the bath can assist in slag foaming. The injection carbon is supplied in the form of petroleum coke, but it typically contains higher carbon content compared to metallurgical coke and anthracite coal. The injection carbon is primarily intended for slag foaming through the generation of CO from the reactions of carbon with the supplied oxygen and/or the FeO in the slag. Good slag foaming helps improve heat transfer from the arc to the bath because it minimizes heat loss through radiation by engulfing the arc. Other sources of carbon include the carbon content in the scrap and the carbon from the graphite electrodes. The carbon content of the scrap contributes chemical energy to the process, foams the slag and helps remove nitrogen from the bath. The carbon from the graphite electrode contributes chemical energy to the bath, but the energy from this process is very minimal. It should be noted that even though the combustion of carbon generates energy, a significant amount of energy is also conveyed away from the furnace into the duct system by the evolving CO.

Understanding how the carbon content of the bath changes with time is important for efficient operation of the EAF. At the early stage of the melting process when the carbon content of the bath is high, the reaction of carbon with oxygen is limited by the transport of oxygen, but as the bath gets depleted of carbon, it gradually transitions into carbon-transport limited. The general rate equation for decarburization can be written as in Eq. 23:

$$\frac{dC}{dt} = -\frac{KA}{V}$$

(Eq. 23)

where

K = mass transfer coefficient of either oxygen or carbon,
A = reaction area and
V = volume of steel.

Upon integration, the decarburization process can be expressed as in Eq. 24:

$$\ln \frac{[\%C] - [\%C]_{eq}}{[\%C]_o - [\%C]_{eq}} = -\frac{KAt}{V}$$

(Eq. 24)

where

$\%C$ = concentration of carbon at time t,
$\%C_0$ = concentration of carbon at the start of decarburization and
$\%C_{eq}$ = equilibrium concentration of carbon.

The bath carbon can be expressed as a function of time, as in Eq. 25:

$$\%C = \left(\%C_0 - \%C_{eq}\right)e^{-\frac{KA}{V}t} + \%C_{eq}$$

(Eq. 25)

Eq. 25 can be used if the mass transfer coefficient and the reaction area can be determined. Needless to say, accurate determination of the mass transfer coefficient and the reaction area is very difficult in an industrial environment. However, by simultaneously solving Eqs. 10 and 23, it was possible to estimate the bath carbon content at any time during the melting and refining processes.

As the carbon content of the bath decreases, its oxygen content rises. Therefore, there is an equilibrium relationship between carbon and oxygen.[40–45] It has been generally assumed that the product of equilibrium concentrations of oxygen and carbon is a constant, and this product is directly proportional to the carbon monoxide pressure in equilibrium with the liquid iron. Vacher et al. determined the value of carbon-oxygen product over a wide range of concentrations at a constant temperature and one atmospheric pressure of carbon oxides in a high-frequency induction furnace. The determined values for carbon-oxygen product range from 0.001 to 0.006. A relationship between carbon and oxygen (shown in Eq. 26) was proposed for data acquired from the LD plant. Other studies conducted in the basic oxygen process suggests a non-equilibrium relationship between carbon and oxygen (shown in Eq. 27) at carbon contents of <0.05 wt.%.[44] Since it is not clear if any of the two equations are applicable to the EAF steelmaking process, one of the objectives of this study was to establish a relationship between carbon and oxygen in the EAF steelmaking process by performing tests to determine the carbon and oxygen contents of heats just before tapping. The results of such tests will be discussed later in the paper.

$$[\%C][\%O] = const.$$

(Eq. 26)

$$\sqrt{[\%C]}[\%O] = const.$$

(Eq. 27)

Chemistries of Silicon, Aluminum and Manganese — The starting concentrations of Si, Al and Mn in the bath were computed from the chemistry of each scrap type in the scrap recipe. By solving Eqs. 11–15, the rates of oxidation of these elements were determined. This allows the determination of the changes in the concentrations of these elements at any time during the melting and refining processes.

Slag Chemistry Prediction Module — The slag composition depends on the amounts of supplied slag formers, oxidation of the dissolved elements in the scrap, the gangue contents of the scrap, and erosion of the furnace refractory. In this model, slag composition is predicted based on the amount of slag formers used, gangue contents of the scrap and oxidation of dissolved elements. The rate of erosion of the furnace refractory is difficult to estimate, but its contribution to the slag is considered insignificant.

Unlike for intermediary raw materials, such as hot briquetted iron (HBI) and direct reduced iron (DRI), the gangue contents of scrap are usually not known. In addition, prolonged storage of scrap can dramatically change its gangue contents. Therefore, for recycled scrap, certain constant values of gangue content were used in this model.

The weight of slag at any given time is calculated in accordance to Eq. 28:

$$\sum_{i=1}^{m} M_{S_i} = M_{sf} + \sum_{i=1}^{k} M_{FeO_i} + \sum_{i=1}^{l} M_{FeO_{Sc_i}}$$
$$+\sum_{i=1}^{n} M_{CaO_{Sc_i}} + \sum_{i=1}^{p} M_{SiO_{Sc_i}} + \sum_{i=1}^{q} M_{MgO_{Sc_i}} + \sum_{i=1}^{u} M_{Al_2O_{3\,Sc_i}}$$
$$+\sum_{i=1}^{\nu} M_{MnO_i} + \sum_{i=1}^{x} M_{SiO_{2i}} + \sum_{i=1}^{y} M_{Al_2O_{3i}}$$

(Eq. 28)

where

M_{sf} = the total weight of lime and dolo-lime supplied,
M_{FeO}, M_{MnO}, M_{SiO_2} and $M_{Al_2O_3}$ = the weights of FeO, MnO, SiO_2 and Al_2O_3 that form through oxidation reactions,
$M_{FeO_{sc}}$, $M_{CaO_{sc}}$, $M_{SiO_{2sc}}$, $M_{MgO_{sc}}$ and $M_{Al_2O_{3sc}}$ = weights of oxides from the gangue contents of the scrap and
i = time.

Model Outputs

The model was programmed using C#. Data inputs are provided every 10 seconds, and this allows rapid computing and display of outputs in a timely manner for use by the operators. For on-line implementation of the model for process optimization by the EAF operators, the most important output parameters that can be of value to the operators are bath temperature, bath carbon content, bath oxygen content, slag composition, and bath chemistry, including carbon, oxygen, silicon and manganese.

Prediction of Bath Temperature — The bath temperature is determined by solving Eqs. 19 and 20. Figs. 2a and 2b are examples of the predicted and measured bath temperatures for heats made with one charge and two scrap charges, respectively. It can be seen that for these heats, the predicted and measured bath temperatures closely matched each other. However, the accuracy of the predicted temperature depends on the accuracy of the input materials. For example, the measured scrap charge weight may deviate from the actual weight in the furnace due to errors resulting from weighing equipment. The other factor is the inability to precisely determine the hot heel in the furnace. For this model, a certain constant value was used for the hot heel. As a result of these unknowns, as shown in Fig. 3, the predicted bath temperatures can deviate from the measured values by up to 200°F. However, for most of the heats, the deviation between the model and measured values is between 0 and 100°F.

Prediction of Bath Carbon Content — As stated earlier, the change in the carbon content of the bath is determined by solving Eqs. 10 and 25. At the early stage of the refining process, the rate of change in carbon

Figure 2

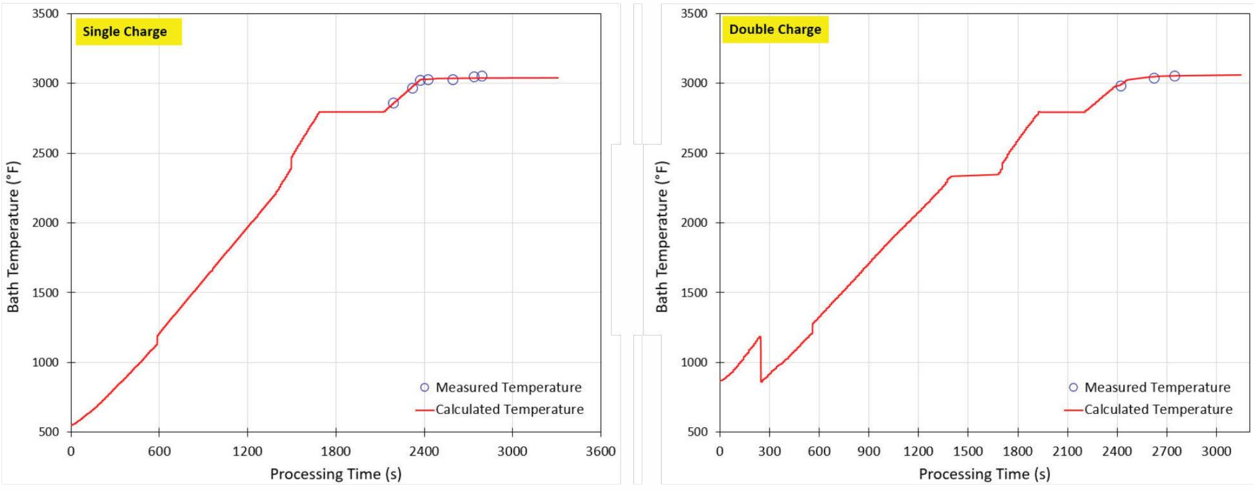

(a) (b)

Predicted vs. measured bath temperature as function of time: (a) single scrap charge and (b) double scrap charge.

Figure 3

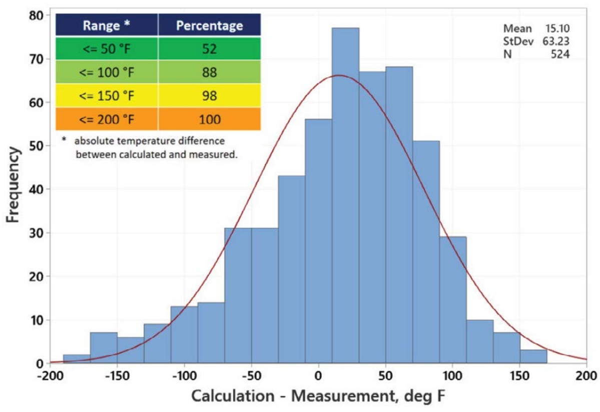

Range *	Percentage
<= 50 °F	52
<= 100 °F	88
<= 150 °F	98
<= 200 °F	100

* absolute temperature difference between calculated and measured.

Histogram of the difference in predicted and measured bath temperatures.

Figure 4

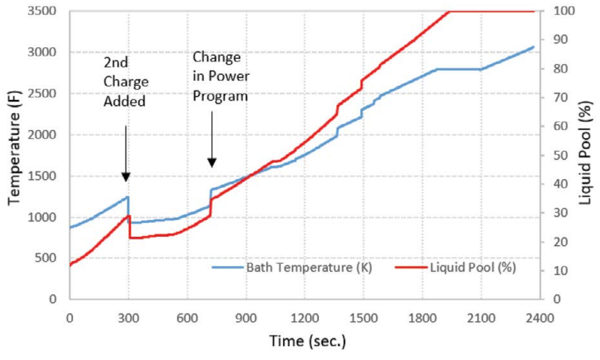

Change in bath temperature and liquid pool with time.

Figure 5

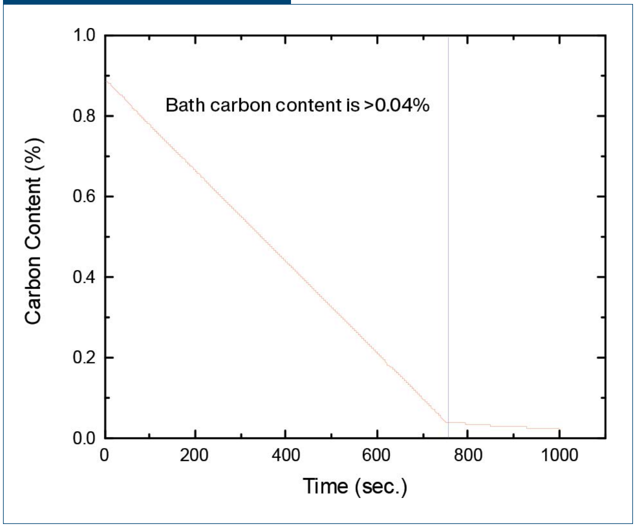

Change in bath carbon content with time during refining.

content is very high. Once the carbon content decreases to certain levels, the rate of combustion of carbon slowed down. Fig. 5 is an example of the change in the bath carbon content during the refining period. Figs. 6a and 6b compare the predicted bath carbon contents to Celox and LECO carbon contents for heats with and without charge carbon additions, respectively. It can be seen that, in both cases, the predicted bath carbon contents match more closely to the measured bath carbon with LECO Instrument compared to the carbon contents determined by Celox readings. The bath carbon prediction accuracy is affected by the uncontrolled variation in the recovery rate of the supplied carbon.

Prediction of Bath Oxygen Content — Some limited experiments were conducted to determine the bath carbon and oxygen contents with the LECO instrument. The results show that carbon and oxygen obey an exponential decay relationship, as shown in Fig. 7. The exponential decay relationship was adopted for use in predicting the bath oxygen content at any given time during the melting and refining processes. Thus, the relationship of oxygen to carbon can be written as shown in Eq. 29:

$$O(\text{ppm}) = 2244.6e^{-18.01\%C}$$

(Eq. 29)

Predicting Silicon, Manganese and Aluminum Contents — The predicted changes in the concentrations of silicon, aluminum and manganese during the melting and refining processes are shown in Fig. 8. The oxidation rate of these elements is divided into two periods. Initially, when the bath carbon is very high, no appreciable change in the contents of these elements occurred, but as the bath becomes depleted of carbon and more oxygen becomes available for their oxidation, there is a steep decline in the concentrations of these elements.

Predictions of Slag Composition — A slag index (phosphate capacity index) was developed to evaluate slag foaming and efficiency of phosphorus removal. The formula derived for phosphate capacity index was reported in a previous publication.[46] Fig. 9 shows the relationship between the distribution ratio of phosphorus in slag to steel and phosphate capacity index. It is apparent from Fig. 9 that there is an optimal

Figure 6

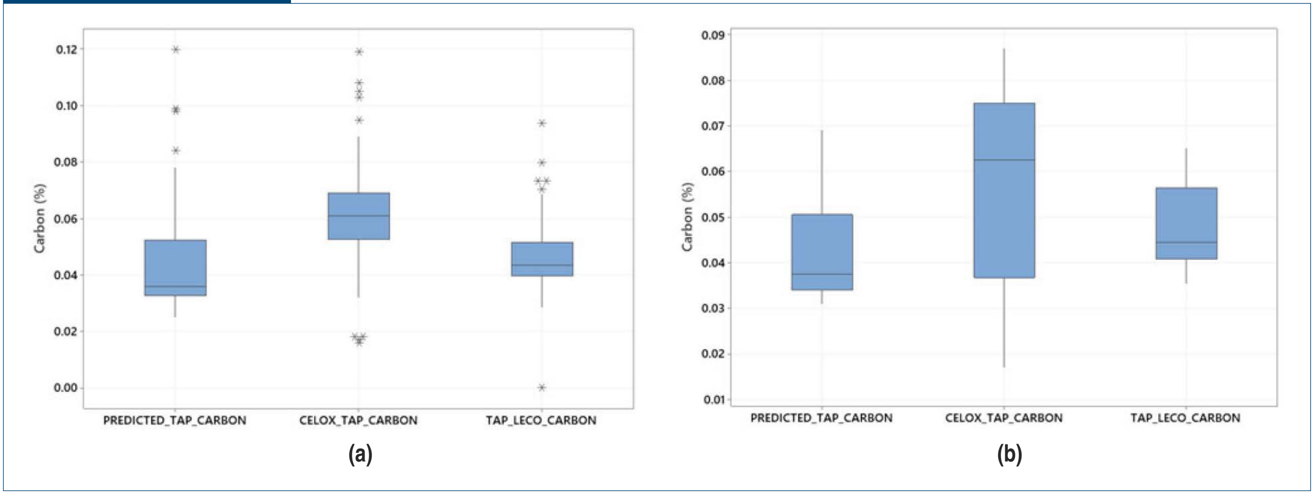

Predicted vs. measured bath carbon content: (a) heats with charge carbon and (b) heats without charge carbon.

Figure 7

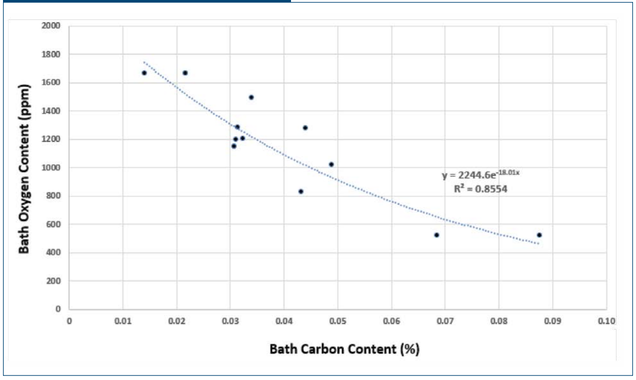

Bath carbon content vs. bath oxygen content.

Figure 8

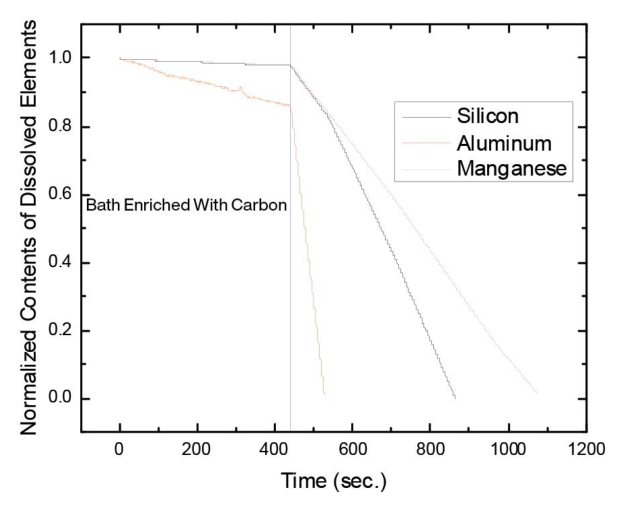

Changes in the bath contents of silicon, aluminum and manganese vs. time.

range of phosphate capacity index for a maximum slag-steel phosphorus distribution ratio. At SSAB Iowa, the slag formers are gradually injected into the bath during the melting process. The model begins to predict slag composition once the bath temperature is high enough for liquid slag to begin to form. For this model, the liquidus temperature of slag was taken as 1,573 K.[13] Initially, the slag is enriched with FeO due to the inherent oxide layer in the scrap. The FeO content of the slag increases as the FeO gradually gets transferred from the scrap into the bath and with oxidation from the supplied oxygen. As the rates of injection of slag formers increase and oxidation of Si and Al intensifies, the FeO content decreases, and then it begins to rise again once the bath is depleted of Si and Al and additions of slag formers have been terminated. The change in slag composition with time allows for evaluation of different constituents of the slag-on-slag fluidity during the course of EAF steelmaking. An example of changes in slag composition with time is shown in Fig. 10. It can be seen from Fig. 10 that there is a tendency of the slag phosphate capacity index to decrease toward the end of refining. Therefore, to avoid phosphorus reversion, prolonged refining time should be avoided. Fig. 11 compares the predicted slag composition to the measured slag composition at the end of refining in the EAF. The predicted values are very close to the measured values.

The relationship between slag volume and phosphate capacity index was evaluated. It was determined

Figure 9

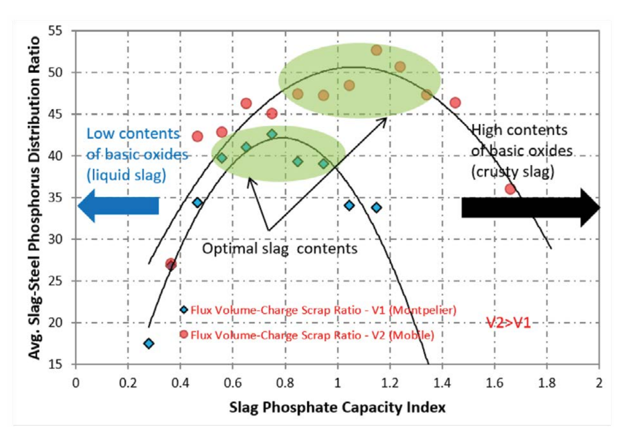

Slag-steel phosphate distribution ratio vs. phosphate capacity index.

Figure 10

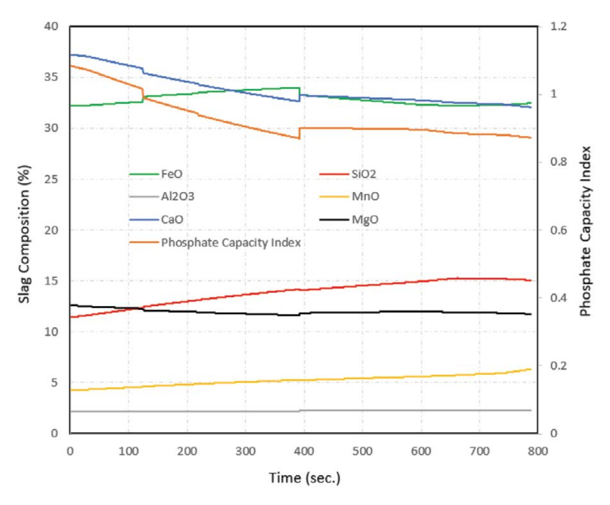

Change in slag composition with time.

that when the slag volume is excessive, the slag tends to be enriched with FeO, leading to low phosphate capacity index (see Fig. 12). Thus, the slag submodel can be used for slag engineering to improve phosphorus removal efficiency and slag foaming, and ensure more efficient operation of the EAF.

Figure 11

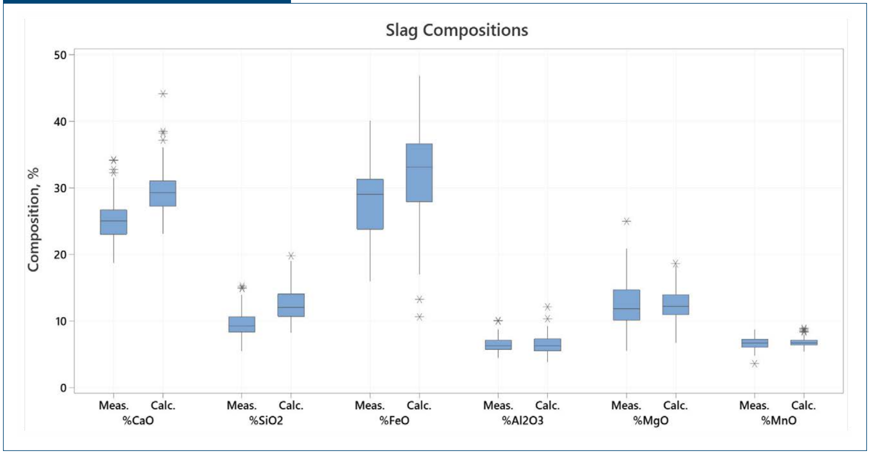

Predicted vs. measured slag composition.

Figure 12

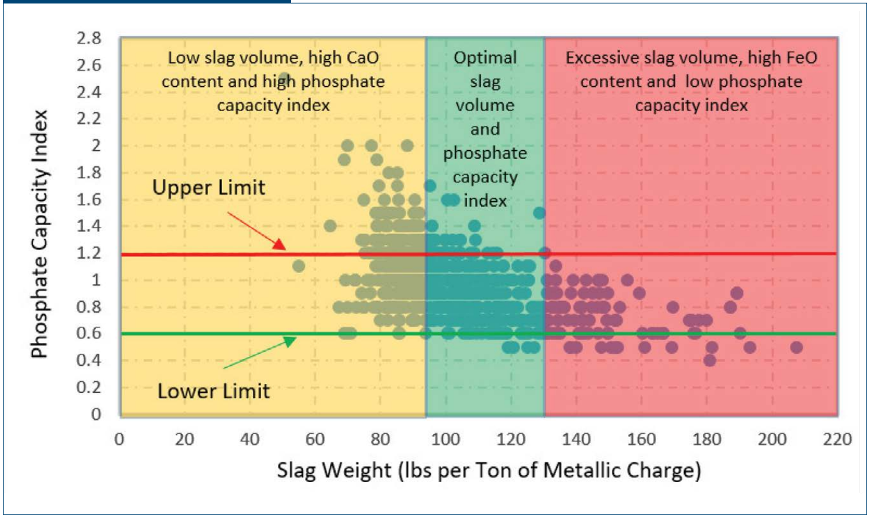

Slag phosphate capacity index vs. slag volume.

Conclusions

A comprehensive and dynamic thermodynamic model was developed for the scrap melting process at SSAB Iowa. The model comprises of four submodels that include predictions of bath temperature, bath carbon and oxygen contents, changes in the contents of dissolved elements and slag composition. The model was integrated with the level 1 control system to provide live data for use as guidelines for on-line process control during melting and refining processes in the EAF.

Acknowledgments

The authors would like to thank Ben Kowing and other SSAB Americas' senior managers for supporting this project. Special thanks go to Miles Haberkorn of SSAB for collecting some of the process data used for the calibration of the model. The authors are grateful to the Montpelier Operations for working with them to implement the model for on-line use by the operators.

References

1. *The Story of Electricity,* T.C. Martin and S.L. Coles, eds., New York, N.Y., USA, 1919, pp. 503–550.
2. H. Walde, "Recent Developments in Arc-Furnace Design and Power Supply," *The Iron and Steel Inst. Conference in Sheffield,* 1964, pp. 94–104.
3. J.R. Bello, "Recent Developments in Arc-Furnace Electrode Regulation," *The Iron and Steel Inst. Conference in Sheffield,* 1964, pp. 105–118.
4. T. Emi, "Steelmaking Technology for the Last 100 Years: Toward Highly Efficient Mass Production Systems for High Quality Steels," *ISIJ Int.,* Vol. 55, No. 1, 2015, pp. 36–66.
5. "Commentary: Electric Arc Furnace Scrap Preheating," The EPRI Center for Materials Production, Carnegie Mellon Research Inst., Pittsburgh, Pa., USA, 1997, pp. 1–4.
6. *Techcommentary: Understanding Electric Arc Furnace Operations for Steel Production,* The Center for Metals Production — An EPRI-Sponsored R&D Applications Center, Vol. 3, No. 2, 1987.
7. A.D. Willis, "Innovative Conservation Through Scrap Pre-Heating in an Electric Arc Furnace," *2013 ACEEE Summer Study on Energy Efficiency in Industry,* 2013.
8. M.C. Mantovani, C. Takano and P.M. Buchler, "EAF and Secondary Dust Characterization," *Ironmaking and Steelmaking,* Vol. 34, No. 4, 2004, pp. 325–332.
9. S. Wannakamb, S. Manuskijsamrun and W. Buggakupta, "The Use of Electric Arc Furnace Dust From Steel Recycling in Ceramic Glaze," *Suranaree J. Sci. Technol.,* Vol. 20, No. 4, 2013, pp. 329–337.
10. W.E. Schwabe, "Power Control Factors in Electric Arc Furnaces," *Proceedings of Electric Furnace Conference,* 1963, pp. 141–156.
11. R.S. Howes, "Production of Open-Hearth Quality Steels in Large Arc Furnaces," *Steelmaking in Basic Arc Furnace, The Iron and Steel Inst. Conference in Sheffield, U.K.,* 1964, pp. 78–81.

12. V.Y. Risonarta, L. Voj, H. Pfeifer, H.P. Jung and S. Lenz, "Optimization of Electric Arc Furnace of Deutsche Edelstanlwerke," *Archives of Metall. and Mater.,* Vol. 53, Issue 2, 2008.
13. S. Abraham, "Physico-Chemical Analysis of Technological Processes of Melting Steel in 100 Tonne Electric Arc Furnace With Continuous Feeding of Hot Briquetted Iron," thesis, Moscow State Institute of Steel and Alloys, Russia, 1993.
14. S. Abraham and S. Chen, "EAF Energy and Material Balance Modeling," *Iron & Steel Technology,* 2008, pp. 32–40.
15. H. Saint-Raymond, D. Huin and F. Stouvenot, "Mechanisms and Modeling of Liquid Steel Decarburization Below 10 ppm Carbon," *Mater. Trans.,* JIM, Vol. 41, No. 1, 2000, pp. 17–21.
16. H. Sun and R.D. Pehlke, "Modeling and Experimental Study of Gaseous Oxidation of Liquid Iron Alloys," *Metall. and Mater. Trans. B,* 1996, pp. 854–864.
17. T. Meier, K. Gandt, T. Echterhof and H. Pfeifer, "Modeling and Simulation of the Offgas in an Electric Arc Furnace," *Metall. and Mater. Trans. B,* 2017, pp. 3329–3344.
18. J. Jones, P. Safe and B. Wiggins, "Optimization of EAF Operations Through Offgas System Analysis," *Electric Furnace Conference Proceedings,* 1999, pp. 459–480.
19. D. Guo and G.A. Irons, "Modeling of Scrap Melting in an Electric Arc Furnace," *ICS Proceedings,* 2005, pp. 441–448.
20. S.A. Matson and W.F. Ramirez, "The Dynamic Modeling of an Electric Arc Furnace," *Electric Furnace Conference Proceedings,* 1997, pp. 675–685.
21. M. Kvačič, K. Stopar, R. Vertnik and B. Šarler, "Comprehensive Electric Arc Furnace Electric Energy Consumption Modeling: A Pilot Study," *Energies,* Vol. 12, No. 2142, 2019, pp. 1–13.
22. B. Boulet, G. Lalli and M. Ajersch, "Modeling and Control of an Electric Arc Furnace," *Proceedings of the American Control Conference,* 2003, pp. 3060–3064.
23. Ü. Çamdali and M. Tunç, "Modeling of Electric Energy Consumption in the AC Electric Arc Furnace," *Int. Energy Res.,* Vol. 26, 2002, pp. 935–945.
24. A. Fathi, Y. Saboohi, I. Škrjanc, and V. Logar, "Comprehensive Electric Arc Furnace Model for Simulation Purposes and Model-Based Control," *Steel Res. Int.,* Vol. 83, No. 3, 2017, pp. 1–22.
25. M. Kirschen, K. Badr and H. Pfeifer, "Influence of Direct Reduced Iron on the Energy Balance of the Electric Arc Furnace in Steel Industry," *Energy,* Vol. 36, 2011, pp. 6146–6155.
26. V. Logar, D. Dovžan and I. Škrjanc, "Modeling and Validation of an Electric Arc Furnace: Part 1, Heat and Mass Transfer," *ISIJ Int.,* 2012, Vol. 52, No. 3, pp. 402–412.
27. V. Logar, D. Dovžan and I. Škrjanc, "Modeling and Validation of an Electric Arc Furnace: Part 2, Thermo-Chemistry," *ISIJ Int.,* 2012, Vol. 52, No. 3, pp. 413–423.
28. R.D. M. MacRosty and C.L.E. Swartz, "Dynamic Optimization of Electric Arc Furnace Operation," *AIChE J.,* 2007, Vol. 53, No. 3, pp. 640–653.
29. R.D. M. MacRosty and C.L.E. Swartz, "Dynamic Modeling of an Industrial Electric Arc Furnace," *Ind. Eng-Chem. Res.,* 2005, Vol. 44, pp. 8067–8083.
30. R.D. Morales, H. Rodríguez-Hernandez and A.N. Conejo, "A Mathematical Simulator for the EAF Steelmaking Process Using Direct Reduced Iron, *ISIJ Int.,* Vol. 41, 2001, No. 5, pp. 426–435.
31. R.D. Morales, A.N. Conejo and H.H. Rodríguez, "Process Dynamics of Electric Arc Furnace During Direct Reduced Iron Melting," *Metall. and Mater. Trans. B,* Vol. 33B, 2002, pp. 187–199.
32. H.J. Odenthal, A. Kemminger, F. Krause, L. Sankowski, N. Uebber and N. Vogl, "Review on Modeling and Simulation of the Electric Arc Furnace (EAF)," *Steel Res.,* Vol. 89, 2018, pp. 1–36.
33. F. Opitz and P. Treffinger, "Physics -Based Modeling of Electric Operation, Heat Transfer, and Scrap Melting in an AC Electric Arc Furnace," *Metall. and Mater. Trans. B,* Vol. 47B, 2016, pp. 1489–1503.
34. Y. Chen, A.K. Silaen and C.Q. Zhou, "3D Integrated Modeling of Supersonic Coherent Jet Penetration and Decarburization in EAF Refining Process," *Processes,* Vol. 8, No. 700, 2020, pp. 1–18.
35. L.S. Carlsson, P.B. Samuelsson and P.G. Jonsson, "Predicting the Electrical Energy Consumption of Electric Arc Furnaces Using Statistical Modeling," *Metals,* Vol. 9, No. 959, 2019, pp. 1–33.
36. L. Carlsson, "Applied Machine Learning in Steel Process Engineering — Using Supervised Machine Learning Models to Predict the Electrical Energy Consumption of Electric Arc Furnaces," thesis, KTH, Sweden, 2021.
37. C. Chen, Y. Liu, M. Kumar and J. Qin, "Energy Consumption Modelling Using Deep Learning Technique — A Case Study of EAF," *Procedia CIRP,* 2018.
38. E.J. Evenson and M.J. Kempe, "Neural Network Modeling and Heuristic Control for Electric Arc Furnace Process Optimization," *Process Technology Conference Proceedings,* 1998, pp. 675–687.
39. J.J. Valencia and P.N. Quested, *Thermo-Physical Properties,* ASM International, 2008, pp. 468–481.
40. M.Y. Solar and R.I.L. Guthrie, "Kinetics of the Carbon-Oxygen Reaction in Molten Iron, *Metall. Trans.,* Vol. 3, pp. 713–722.
41. F.J. Mannon and R.J. Fruehan, "Decarburization Kinetics of Liquid Fe-Csat Alloys by CO_2," *Metall. Trans. B,* pp. 853–861.
42. N.H. El-Kaddah and D.G.C. Robertson, "Equilibria in Reactions of CO and CO_2 With Dissolved Oxygen and Carbon in Liquid Iron," *Metall. Trans. B,* 1977, pp. 569–579.
43. N.H. El-Kaddah and D.G.C. Robertson, "The Kinetics of Gas-Liquid Metal Reactions Involving Levitated Drops. Carburization and Decarburization of Molten Iron in CO-CO_2 Gas Mixtures at High Pressures," *Metall. Trans. B,* Vol. 9B, 1978, pp. 191–199.
44. E.T. Turkdogan, *Fundamentals of Steelmaking,* The Inst. of Mater., 1996, pp. 217–235.
45. H.C. Vacher and E.H. Hamilton, "The Carbon-Oxygen Equilibrium in Liquid Iron," New York Meeting, 1931, pp. 124–130.
46. S.O. Abraham, Y. Wang, R. Petty, T. Franks, T. Sprague, G. Brown, W. Woods, W. Nicholson, M. Haberkorn and R. Bodnar, "Slag Engineering for Phosphorus Removal in the EAF and Sulfur Removal in the Ladle," *Iron & Steel Technology,* 2020, pp. 72–82. ✦

This paper was presented at AISTech 2021 — The Iron & Steel Technology Conference and Exposition, Nashville, Tenn., USA, and published in the AISTech 2021 Conference Proceedings.